PAPER

Ab initio-informed phase-field modeling of dislocation core structures in equal-molar CoNiRu multi-principal element alloys

To cite this article: Yanqing Su et al 2019 Modelling Simul. Mater. Sci. Eng. 27 084001

View the article online for updates and enhancements.

Recent citations

- <u>Local slip resistances in equal-molar MoNbTi multi-principal element alloy</u> Shuozhi Xu *et al*
- The effect of local chemical ordering on Frank-Read source activation in a refractory multi-principal element alloy Lauren T.W. Smith et al
- Atomistic calculations of the generalized stacking fault energies in two refractory multi-principal element alloys
 Shuozhi Xu et al



Ab initio-informed phase-field modeling of dislocation core structures in equal-molar CoNiRu multi-principal element alloys

Yanqing Su¹, Shuozhi Xu² and Irene J Beyerlein^{1,2,3}

E-mail: yanqingsu@ucsb.edu

Received 9 March 2019, revised 7 August 2019 Accepted for publication 15 August 2019 Published 30 August 2019



Abstract

In this work, selecting the equal-molar CoNiRu multi-principal element alloy (MPEA) as a model material, we study dislocation core structures starting from first principles. We begin by sifting through all possible configurations to find those corresponding to elastic stability and energetically favored facecentered cubic (fcc) phases and, then, for these configurations, employ a phase field-based model to predict the extent of dislocations lying within them. The main findings are that for the fcc phase, (i) large variations in atomic configuration for the same chemical composition can cause significant changes in the generalized stacking fault energy surface and (ii) the dispersion in defect fault energies are chiefly responsible for substantial variations in the intrinsic stacking fault (ISF) widths of screw and edge dislocations. For instance, positive the ISF energy can vary by 10 times, with the lower values correlated with entirely Ni and Ru atoms and higher values with only Co and Ru atoms across the slip plane. Variations in lattice parameter and stiffness tensor accompany local differences in atomic configuration are also taken into account but shown to play a lesser role. We find that the dislocation can experience profound variations (3-7-fold changes) in its associated ISF width along its line, with the screw dislocation experiencing a greater variation than the edge dislocation (6.02-43.22 Å for the screw dislocation, and 19.6-62.62 Å for the edge dislocation). We envision that the ab initio -informed phase-field modeling method developed here can be readily adapted to MPEAs with other chemical compositions.

¹ Department of Mechanical Engineering, University of California, Santa Barbara, Santa Barbara CA 93106-5070, United States of America

² California NanoSystems Institute, University of California, Santa Barbara, Santa Barbara, CA 93106-6105, United States of America

³ Materials Department, University of California, Santa Barbara, Santa Barbara CA 93106-5050, United States of America

Keywords: multi-principal element alloy, density functional theory, phase-field modeling, dislocation

(Some figures may appear in colour only in the online journal)

1. Introduction

The field of multi-principal element alloys (MPEAs) has seen explosive development since its inception in 2004 [1, 2]. MPEAs exhibit high strength levels at high temperatures, excellent fracture toughness at low temperatures, outstanding strength-ductility combination, as well as superior hardness and specific strength [3].

Unlike traditional metallic alloy systems that are based on one or two principal elements and many additional elements in dilute concentrations, MPEAs consist of three or more principal metallic elements, with nearly equal atomic percentages [4]. At an atomic level, the element locations are randomly distributed, leading to fluctuations in local concentrations, atomic arrangements, and lattice distortions [5–7]. How the local randomness gives rise to superior structural properties, far superior than those of traditional alloys, still remains to be fully understood.

Like in pure metals and traditional alloys, experiments have observed that the mechanisms of plastic deformation in face-centered cubic (fcc) MPEAs involve dislocation slip and deformation twinning [8–10]. For fcc materials in general, understanding of the properties of the dislocation cores, such as its size, is essential. The extent or width of the dislocation core affects many elementary dislocation processes, such as formation, annihilation, storage, climb, and the dominating plastic deformation mechanism (e.g. slip or twinning) when the metal is strained. Nearly every structural metallic property, such as strength, ductility, creep, and fatigue, is determined by the mobility and storage of dislocations. Thus, quantitative understanding of how variations in material properties affect dislocation core structures and the prevailing plastic deformation mechanisms could greatly benefit processing and design of MPEAs.

Dislocation core structures in fcc crystals are multiscale in nature owing to the short-range core interactions and long-range elastic fields [11]. The low energy, stress-free size of the core of a perfect dislocation within the slip plane can extend in the range of 1-10 nm, depending on the metal. The Burgers vector of the dislocation dissociates into two partial dislocations, each with a shorter Burgers vector, and glissile on the same {111} slip plane. Their elastic fields repel one another, which encourages them to glide apart, again on the same plane. Their glide motion creates an intrinsic stacking fault (ISF) in between them. The energetic expense in creating the fault inhibits the two partials from splitting infinitely. The finite equilibrium distance they spread apart can be approximated by a force balance between the attraction that tends to shrink the fault and the repulsion between the two partials. When the final structure of the core can be assumed *a priori* to consist of these two partials with an ISF in between, the ISF width d can be roughly estimated using linear elastic, isotropic dislocation theory [12] to be:

$$d_{\rm scr} = \frac{\mu b^2}{24\pi\gamma_{\rm ief}} \frac{2 - 3\nu}{1 - \nu},\tag{1}$$

$$d_{\rm edg} = \frac{\mu b^2}{24\pi \gamma_{\rm isf}} \frac{2+\nu}{1-\nu}$$
 (2)

for screw and edge dislocations, respectively, where b is the magnitude of the Burgers vector of a full dislocation, μ is the isotropic shear modulus, ν is the isotropic Poission's ratio, and $\gamma_{\rm isf}$ is the surplus potential energy per unit area associated with the ISF.

In an fcc MPEA, random concentration fluctuations could lead to spatial variations in elastic modulus, lattice parameter, and $\gamma_{\rm isf}$, bringing complexity to dislocation core structures and plastic deformation [13]. In recent years, many experimental and atomic-scale calculations have studied these variations. Atomic-level modeling [14] and transmission electron microscopy experiments [15] found that, in fcc MPEAs, a dislocation usually attains wavy-configuration as it moves through a random field of solutes due to a combined effect of significant core structure variations along the dislocation line and strong kink pinning. Recent atomistic simulations showed a threefold variation in the ISF width in a model fcc MPEA [16].

Several mesoscale, multiscale computational models employing energy relaxation methods have been used to predict the dissociation event to the final low energy core structures, when starting with compact, perfect (i.e. undissociated) dislocations. These include models based on either the phase-field (PF) method [17] or the generalized Peierls-Nabarro (GPN) model [18]. Calculations from these models have suggested that the local compositional randomness in MPEAs mainly contributes to the higher strength over their singlecomponent counterparts, and the substitutional solid-solution strengthening is the main strengthening mechanism of single-phase fcc MPEAs [4]. To model the dislocation core, they represent the atomic-level spatial variations in the energy associated with fault formation, that is, the generalized stacking fault energy (GSFE) curve, while at the same time, assuming that the elastic response was uniform across the crystal and isotropic. For the GSFE curve, a oneterm or two-term sinusoidal function is commonly used and the parameters associated with these functions were informed by molecular static (MS) calculations using empirical potentials. In the case of pure fcc metals, it has been shown that PF/GPN models can provide dislocation core predictions in better agreement with core widths from atomistic calculations, when the variation in potential energy with all possible in-plane shear displacements was taken into account [19–21], not just γ_{isf} , which is a local minimum along the GSFE curve, and more generally within the two-dimensional GSFE surface [22]. However, a new analytic dislocation model developed by Szajewski et al [23], which incorporated elastic anisotropy and partial core widths, was able to predict ISF widths in good agreement with only using the γ_{isf} .

In this work, we present a multiscale *ab initio*-informed PF dislocation model to study dislocations in MPEAs, and apply it to calculate the distribution in the ISF widths of screw and edge dislocations in an equal-molar CoNiRu MPEA with an fcc crystal structure. We use density functional theory (DFT) to calculate the lattice parameters, stiffness tensors, and GSFE surfaces associated with all possible atomic configurations of these three elements. For each configuration associated with a stable fcc phase, the individual properties are used as input into a phase-field dislocation dynamics (PFDD) model [24], which accounts for elastic anisotropy, the full parameterized GSFE surface, and the gradient energy term. The lattice parameter and elastic moduli are shown to be insensitive to the local atomic configuration. In contrast, the variation in the GSFE surfaces, and corresponding dislocation core widths is found to be profound, varying up to 7–8 times. Yet, in comparison, we show that the analytical model would significantly overestimate the dispersion in the core width when given the same dispersion on γ_{isf} . We envision that the multiscale model presented here can be

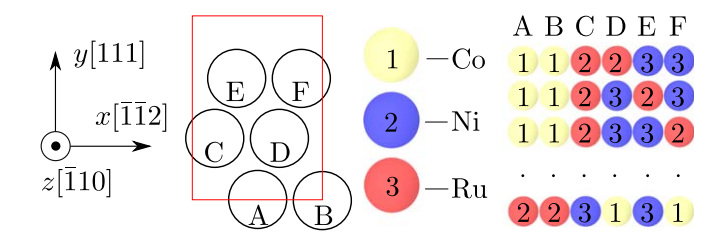


Figure 1. Illustrations of some configurations of equal-molar CoNiRu when a super cell contains 6 fcc lattice sites.

applied to understand the static and moving dislocations in MPEAs, comprised of any number and combination of elements and compositions.

The paper is structured as follows. We begin in section 2.1 by describing the DFT calculations and first and foremost identifying all possible atomic configurations for a given super cell size. Next, in section 2.2, procedures used in the DFT calculations to obtain material properties are detailed. We then follow with the DFT results in section 3, with particular focus on identifying those configurations associated with mechanically stable moduli and fcc phases for subsequent PFDD calculations of core structures. We will show that the DFT calculations suggest that equal-molar CoNiRu MPEAs would consist of a mixed fcc and hexagonal close-packed (HCP) phases. Then, in section 4, the PFDD model formulation and incorporation of the DFT data will be presented [24]. We end with report of the static core structures of screw and edge dislocations, including discussion on the effects of local chemical variation, elastic anisotropy, and the account of gradient energy.

2. DFT calculations

2.1. All possible atomic configurations

The cores of dislocations found in the fcc crystals commonly span length scales in the range of 1–10 nm. For MPEAs, with a given average bulk composition, the local atomic arrangements of the elements can easily vary spatially within this range. With this in mind, we first consider all possible atomic configurations when constructing the model super cells for calculation. These test cases are initialized as an fcc crystal structure with a crystallographic orientations of $x[\bar{1}\bar{1}2]$, y[111], and $z[\bar{1}10]$, as illustrated in figure 1. In a super cell containing N fcc lattice sites, the number of unique atomic configurations for three equal-molar elements $N_{\rm conf}$ is given by:

$$N_{\rm conf} = \frac{\binom{N}{2N/3} \binom{2N/3}{N/3}}{3}.$$
 (3)

According to equation (3), N_{conf} increases rapidly with N. When N=6 and 9, for instance, $N_{\text{conf}}=30$ and 560, respectively. To sufficiently demonstrate the methodology, while bearing in mind the computational expense, we use N=6 in this study. To denote these 30 unique configurations, we let 1, 2 and 3 represent Co, Ni, and Ru atoms, respectively, and arrange the six atoms according to their order, i.e. 112233, 112323, ..., to 223131.

The small system size we use here cannot capture all possible chemical variations in the actual material and corresponds to a high average degree of chemical short-range order (SRO). A much larger-sized random configuration, for instance, would be expected to have

less dispersion in the values of the maxima and minima. DFT calculations in CoCrNi MPEAs by Ding *et al* [25] demonstrated that a larger SRO tends to have higher ISF and unstable stacking fault (USF) energies. DFT calculations in NiFe revealed that a smaller in-plane ISF area leads to a larger standard deviation in the ISF energy [26]. In the present case, we may expect the variation in ISF and USF energies and ISF widths to serve as a conservative estimate of the actual variation in the material. In principle, however, the *ab initio*-informed PFDD framework we present here can accept any number of GSFE surfaces corresponding to a broader range of atomic configurations and chemical compositions.

2.2. Numerical details

DFT calculations are carried out using VASP [27] to determine the lattice parameters, stiffness tensors, and fault energies for all 30 atomic configurations. Within the framework of the projector augmented wave method [28, 29], a pseudopotential is used to approximate the core electrons and a plane-wave basis for the valence electrons. The exchange-correlation energy functional is approximated by the Perdew–Burke–Ernzerhof formulation of the generalized gradient approximation [30]. For the electronic self-consistent loop, the conjugate gradient algorithm is employed. Convergence is reached when the changes in both the total free energy and band structure energy between two steps are smaller than 10^{-4} eV. For correct handling of the Fermi surface, the Methfessel–Paxton smearing method [31] with 0.2 eV smearing width is adopted. The numbers of valence electrons per atom are 9, 16, and 14 for Co, Ni, and Ru, respectively. The cutoff energy for the plane wave basis set is 551.98 eV. In these calculations, magnetism is neglected, since the contributions of Co and Ni atoms to the static magnetic moment difference between the perfect and faulted lattice in FeCrCoNiMn MPEAs are negligible [32]. We validate this assumption, nonetheless, in section 3.3 by carrying out a few GSFE calculations with magnetism taken into account.

While the foregoing DFT approach applies to all DFT calculations in this paper, some details differ when calculating certain quantities.

To calculate the lattice parameter a_0 , the fcc super cell size is varied, and for each size, the free energy without ionic relaxation is calculated. It follows that a_0 corresponds to the cell size with the smallest free energy, or the total cohesive energy $E_{\rm coh}$ of the six atoms. For these calculations, we adopt a k-point mesh of $13 \times 13 \times 13$ in the Monkhorst–Packs scheme to integrate the Brillouin Zone of the primitive unit cell [33]. After a_0 is determined, the stiffness tensor $\mathbf{C}_{\rm E}$ is calculated via the energy-strain approach provided in AELAS [34].

To calculate the GSFE surface $\gamma_{\rm gsf}$ on a given (111) plane, a super cell containing 24 atoms is built by repeating each configuration four times along the y[111] direction. For most configurations (figure 1), the super cell consists of three (111) planes with distinct atomic arrangements, leading to 90 slip planes in total for which $\gamma_{\rm gsf}$ are calculated. Some configurations, however, e.g. 112323 and 223131, possess only two chemically distinct (111) planes. A vacuum region of 8 Å is then added to each cell along the y direction, creating a series of non-interacting slabs. To apply the shear, the top five or six or seven layers of atoms are displaced by a vector φ within the (111) plane with respect to the bottom seven or six or five layers. The top two and bottom two layers of atoms are fixed, while the remaining eight layers are allowed to relax along the y direction. The ionic relaxation stops when the total energy between two steps is smaller than 10^{-3} eV/atom. For these calculations, $13 \times 1 \times 17$ k-points are used.

The surplus potential energy $\gamma_{\rm gsf}$ associated with a given shear displacement is given by

$$\gamma_{\rm gsf} = \frac{E - E_0}{A_0},\tag{4}$$

where E and E_0 are the relaxed free energies of the faulted and unfaulted systems, respectively, and A_0 is the fault area.

To construct the entire GSFE surface, DFT calculations can be repeated so that the energies associated with all possible in-plane shear displacements φ are obtained. It is not common practice, however, to fully calculate with DFT the entire GSFE surface, due to computational expense. In a GPN model for dislocations in Al, Lu *et al* [35] approximated the GSFE surface by a grid of 480 displacements in DFT. However, in the current work, attaining the full GSFE surface with this level of precision means that $480 \times 90 = 43\,200$ DFT calculations would be needed.

To circumvent the computational expense associated with numerous DFT calculations of fault energies, parameterizations of the GSFE surface have been adopted. For an fcc crystal, in particular, the truncated Fourier series with a relatively small number of coefficients have been used as a continuous function to approximate the discretely calculated GSFE surfaces. Recently, in Al and Au, an 11-term Fourier series function [36] was shown to provide a better representation of the GSFE surfaces and results in better ISF widths compared with a 7-term Fourier series function [37]. Here, we adopt the 11-term Fourier series function.

Assigning $d_{x0} = \sqrt{6} a_0/2$ and $d_{z0} = \sqrt{2} a_0/2$ as the periodic lattice lengths along the $\langle 112 \rangle$ and $\langle 110 \rangle$ directions, respectively, the 11-term Fourier series function takes the following form:

$$\begin{split} \gamma_{\rm gsf} &= c_0 + c_1[\cos(2pd_x) + \cos(pd_x + qd_z) + \cos(py - qz)] \\ &+ c_2[\cos(2qd_z) + \cos(3pd_x + qd_z) + \cos(3pd_x - qd_z)] \\ &+ c_3[\cos(4pd_x) + \cos(2pd_x + 2qd_z) + \cos(2pd_x - 2qd_z)] \\ &+ c_4[\cos(pd_x + 3qd_z) + \cos(pd_x - 3qd_z) + \cos(4pd_x + 2qd_z) \\ &+ \cos(4pd_x - 2qd_z) + \cos(5pd_x + qd_z) + \cos(5pd_x - qd_z)] \\ &+ c_5[\sin(2pd_x) - \sin(pd_x + qd_z) - \sin(pd_x - qd_z)] \\ &+ c_6[\sin(4pd_x) - \sin(2pd_x + 2qd_z) - \sin(2pd_x - 2qd_z)] \\ &+ c_7[\cos(6pd_x) + \cos(3pd_x + 3qd_z) + \cos(3pd_x - 3qd_z)] \\ &+ c_8[\cos(8pd_x) + \cos(4pd_x + 4qd_z) + \cos(4pd_x - 4qd_z)] \\ &+ c_9[\cos(4qd_z) + \cos(6pd_x + 2qd_z) + \cos(6pd_x - 2qd_z)] \\ &+ c_{10}[\cos(6qd_z) + \cos(9pd_x + 3qd_z) + \cos(9pd_x - 3qd_z)], \end{split}$$

where $p = (2\sqrt{6}/3)\pi/a_0$ and $q = 2\sqrt{2}\pi/a_0$ are the magnitudes of the reciprocal lattice vectors, $d_x = d_{x0}\varphi_{\bar{1}\bar{1}2}$, and $d_z = d_{z0}\varphi_{\bar{1}10}$. The 11 coefficients c_i are obtained by fitting the equation above to the 11 GSFE values, including ISF energy $\gamma_{\rm isf}$ and USF energy $\gamma_{\rm usf}$. In this way, only 990 DFT calculations are needed for the 90 GSFE surfaces, a substantial time saving compared to directly calculating the full GSFE surface.

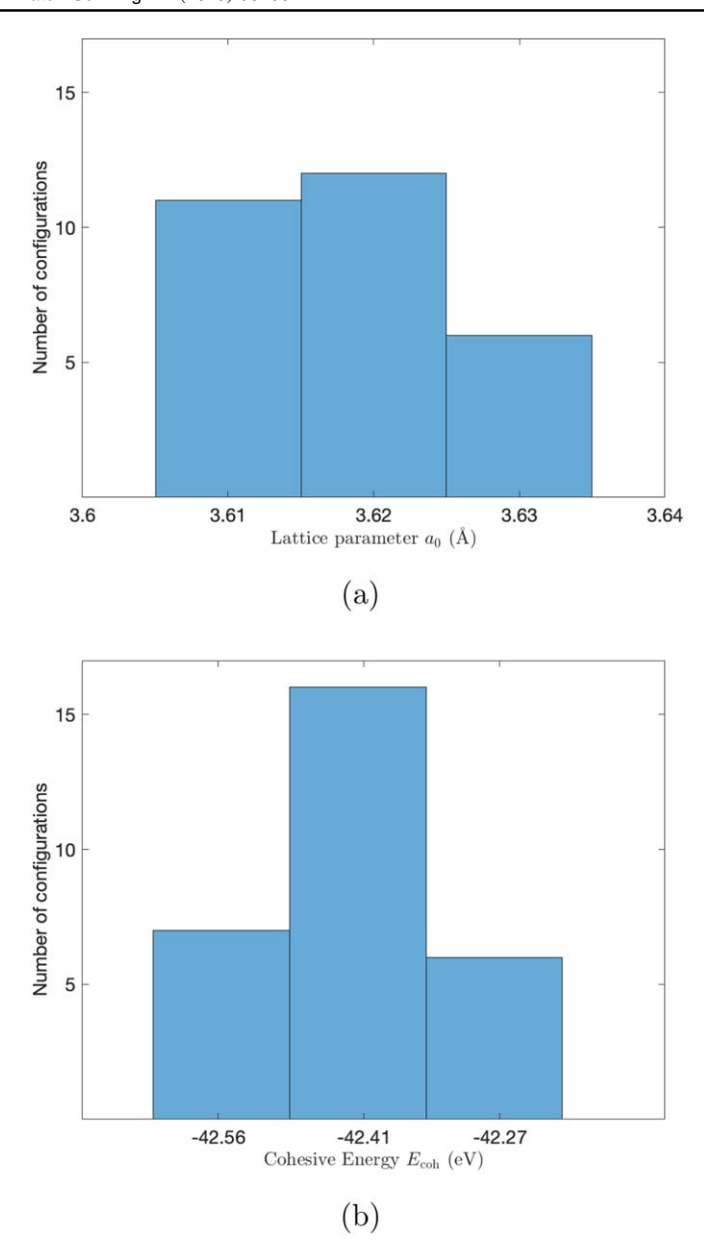


Figure 2. Distributions of the lattice parameter a_0 and cohesive energy $E_{\rm coh}$ of six atoms, among the 30 unique configurations shown in figure 1.

3. DFT results

3.1. Lattice parameter

Figure 2 shows the distributions of a_0 and $E_{\rm coh}$ for all 30 configurations. The variations among the sets of 30 values for these two quantities are small, being less than 0.6%. In these calculations, the super cell is assumed to have six fcc lattice sites. As a result, only one lattice

Table 1. Lattice parameters in fcc system, a_0 (in Å) and in face-centered orthorhombic system, a_x , a_y , a_z (in Å), in selected six-atom structures (illustrated in figure 1) and in a 120-atom SQS.

Configuration	a_0	a_x	a_{y}	a_z	$(a_x + a_y + a_z)/3$
112233	3.63	3.656	3.558	3.657	3.624
121233	3.63	3.646	3.559	3.657	3.621
133221	3.62	3.603	3.608	3.612	3.608
213123	3.62	3.579	3.616	3.644	3.613
SQS	3.61	3.615	3.611	3.605	3.61

parameter a_0 is obtained. On the other hand, in MPEAs, there may exist significant lattice distortion and/or the system may have anisotropic lattice parameters [38]. To validate our results, two additional sets of calculations are conducted. The first set concerns the effects of full relaxation of the simulation cell. In these calculations, four configurations, including 112233, 121233, 133221, and 213123, are considered. The simulation cells are fully relaxed for atomic positions, cell size, and cell shape, such that all components of the stress tensor are zeroed. When the energy minimization is terminated, the four simulation cells are sized/shaped, respectively

$$\begin{bmatrix} 4.47788 & 0.00134 & 0 \\ 0.00188 & 6.16236 & 0 \\ 0 & 0 & 2.58596 \end{bmatrix}, \begin{bmatrix} 4.46562 & -0.00216 & 0 \\ -0.00299 & 6.16419 & 0 \\ 0 & 0 & 2.58305 \end{bmatrix}, \tag{6}$$

$$\begin{bmatrix} 4.41256 & -0.00435 & 0 \\ -0.00614 & 6.24853 & 0 \\ 0 & 0 & 2.55373 \end{bmatrix}, \begin{bmatrix} 4.38304 & -0.02027 & 0 \\ -0.02863 & 6.26298 & 0 \\ 0 & 0 & 2.57662 \end{bmatrix}.$$
 (7)

First, the lattice distortion is negligible (<0.5%) in all cases. Second, given the crystallographic orientations, the three normalized lattice parameters along the x, y, and z directions, respectively denoted as a_x , a_y , and a_z , are summarized in table 1. It is found that the three parameters differ, suggesting that the fully relaxed unit cell has six face-centered orthorhombic sites. However, for each configuration, with the small lattice distortion neglected, the averaged lattice parameter, $(a_x + a_y + a_z)/3$, is close to the one obtained by assuming six fcc lattice sites, a_0 .

To assess the effects of the simulation cell size, we build a 120-atom special quasirandom structures (SQS) [39] of equal-molar CoNiRu MPEAs using ATAT [40]. Once the system structure has fully relaxed, negligible lattice distortion is, again, observed.

Table 1 presents the results of the calculation, where the differences among the three normalized lattice parameters are reduced, compared with those of the six-atom structures. This comparison confirms that bulk equal-molar CoNiRu MPEA has equal lattice parameters. In addition, the averaged lattice parameter of the 120-atom structure is 3.61 Å, and the cohesive energy is 850.143 eV, which corresponds to 7.0845 eV per atom. These values are close to those of the 6-atom structures.

3.2. Stiffness tensor

With a_0 in hand for each configuration, we then calculate the corresponding elastic stiffness tensor. Calculation of $\mathbf{C}_{\rm E}$ requires the material to be elastically stable under a small distortion. This mechanical stability criterion is satisfied for a system constructed of this atomic

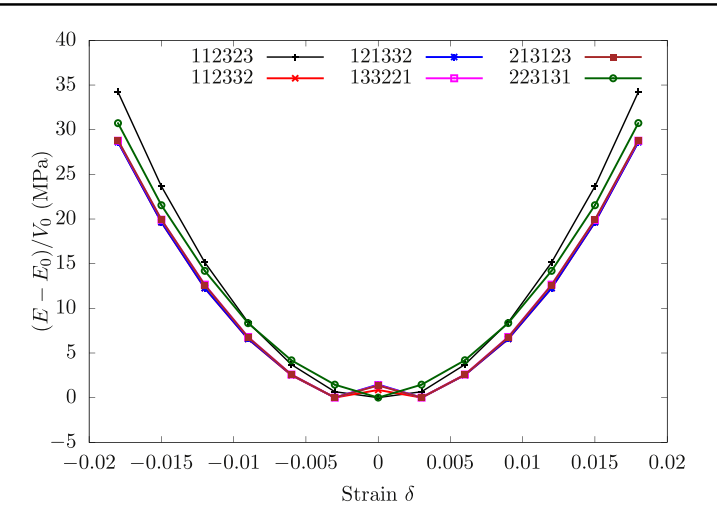


Figure 3. The surplus free energy per unit volume as a result of an applied distortion $\varepsilon=(0,\ 0,\ \delta,\ 0,\ \delta)$ for selected configurations. All are unstable when $\delta=0.003$, except configurations 112323 and 223131.

configuration when the free energy of a distorted material is higher than that of an undistorted one. Otherwise, the system is not stable. Among the 30 configurations, we find that 17 configurations are unstable subject to a small distortion $\varepsilon=(0,\,0,\,0,\,\delta,\,0,\,\delta)$, as shown in figure 3. The reasons may be that the particular configuration does not have a stable fcc structure or it is not fully relaxed. For selected configurations, we fully relaxed the simulation cells (as described in section 3.1) and calculated their strain-energy relation. We find that the mechanical stability remains unchanged regardless of whether the simulation cell is fully relaxed or not. Hence, $\mathbf{C}_{\rm E}$ can only be calculated for the remaining 13 configurations.

For the fcc class of crystal structures, the elastic moduli have three independent constants. However, for such small super cells of equal-molar alloys, the fcc crystalline symmetry can easily be broken [41]. For example, \mathbf{C}_{E} for the second (i.e. 112323) and the last (i.e. 223131) configurations, in the standard x[100], y[010], z[001] framework, are, respectively

To estimate the three independent elastic constants for each fcc atomic arrangement, we calculate the polycrystal elastic constants following [42]

Table 2. Material parameters for the 13 configurations whose stiffness tensor $\mathbf{C}_{\rm E}$ are calculable: lattice parameter a_0 (in Å), polycrystal elastic constants C_{11}^{\dagger} , C_{12}^{\dagger} , C_{44}^{\dagger} (in GPa), isotropic shear modulus in Voigt form $\mu = (3C_{44}^{\dagger} + C_{11}^{\dagger} - C_{12}^{\dagger})/5$ (in GPa), isotropic Poisson's ratio in Voigt form $\nu = (C_{11}^{\dagger} + 4C_{12}^{\dagger} - 2C_{44}^{\dagger})/(4C_{11}^{\dagger} + 6C_{12}^{\dagger} + 2C_{44}^{\dagger})$, elastic anisotropy index $A_{\rm c} = 2C_{44}^{\dagger}/(C_{11}^{\dagger} - C_{12}^{\dagger})$, ISF energy $\gamma_{\rm isf}$ (in mJ m⁻²), and USF energy $\gamma_{\rm usf}$ (in mJ m⁻²). Note that for each configuration, there are three slip planes, and thus three $\gamma_{\rm isf}$ and $\gamma_{\rm usf}$ values. For brevity, we only present values in the last two columns for slip planes where $\gamma_{\rm isf} > 0$ because only these cases are involved in subsequent PFDD simulations. All $\gamma_{\rm isf}$ and $\gamma_{\rm usf}$ values are given in figure 4.

Configuration	a_0	C_{11}^{\dagger}	C_{12}^{\dagger}	C_{44}^{\dagger}	μ	ν	$A_{\rm c}$	$\gamma_{ m isf}$	$\gamma_{ m usf}$
112323	3.61	410.14	171.11	145.1	134.866	0.272	1.21	15.95	396.42
113232	3.61	410.17	171.05	145.13	134.902	0.272	1.21	18.71	395.56
121323	3.61	408.48	170.68	150.93	138.118	0.267	1.27	131.58	530.73
122313	3.61	408.48	170.7	150.89	138.09	0.267	1.27	135.91	534.17
131322	3.61	404.22	170.35	151.87	137.896	0.266	1.3	176.26	747.48
213132	3.61	408.48	170.69	150.9	138.098	0.267	1.27	117.88	506.72
213231	3.61	408.51	170.68	150.9	138.106	0.267	1.27	124.2	513.46
223131	3.61	404.26	170.31	151.91	137.936	0.266	1.3	165.24	725.9
112233	3.63	422.39	146.34	137.76	137.866	0.258	1		
113322	3.63	422.19	146.44	137.68	137.758	0.258	1		
121233	3.63	385.38	165.37	148.56	133.138	0.265	1.35		
122133	3.63	379.62	166.99	141.22	127.26	0.273	1.33		
212133	3.63	385.33	165.41	148.53	133.102	0.265	1.35		

$$C_{11}^{\dagger} = \frac{C_{11} + C_{22} + C_{33}}{3},\tag{10}$$

$$C_{12}^{\dagger} = \frac{C_{12} + C_{13} + C_{23}}{3},\tag{11}$$

$$C_{44}^{\dagger} = \frac{C_{44} + C_{55} + C_{66}}{3}. (12)$$

Table 2 presents these constants, as well as the isotropic shear modulus μ , isotropic Poisson's ratio ν , and elastic anisotropy index for cubic systems A_c , for the 13 stable systems. The combined calculation finds that the variation in μ is relatively small (<4%), and the possible fcc MPEA configurations bear low to medium elastic anisotropy indices. The latter could be anticipated since the HCP Co and Ru are nearly isotropic and $A_c = 2.55$ for fcc Ni [43].

3.3. Generalized stacking fault energies

Two key fault energies that have been shown to influence the ISF width in fcc crystals are the ISF energy $\gamma_{\rm isf}$ and the USF energy $\gamma_{\rm usf}$ [19]. Figure 4 shows the distributions of the $\gamma_{\rm isf}$ and $\gamma_{\rm usf}$ as calculated by DFT for the 90 slip planes. When fitted with a Gaussian distribution, the mean and standard deviation, respectively, in $\gamma_{\rm isf}$ are -44.56 and 101.87 mJ m⁻², and those in $\gamma_{\rm usf}$ are 376.41 and 125.76 mJ m⁻². The mean value of $\gamma_{\rm isf}$ is much smaller than that in pure Ni (144.5 mJ m⁻²) [21], which can be expected for an alloy. Prior experiments in Ni-involved fcc MPEAs have found that $\gamma_{\rm isf}$ decreases as the number of components increases [44]. The standard deviation in $\gamma_{\rm isf}$ is significant. Part of the dispersion naturally arises from the

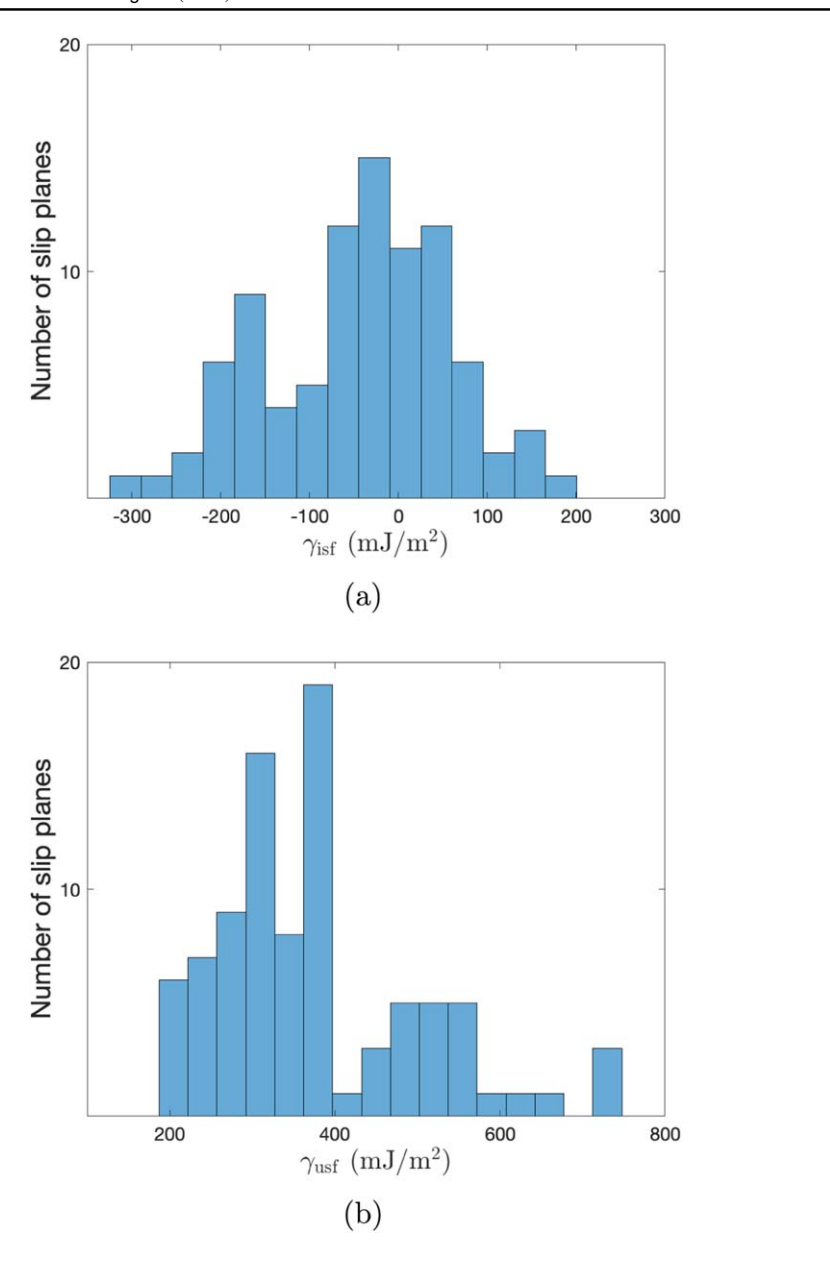


Figure 4. Distributions of ISFE $\gamma_{\rm isf}$ and USFE $\gamma_{\rm usf}$ among the 90 slip planes.

difference in atomic make up of the plane among the different configurations. Another contribution stems from the small super cell size, which includes only six atoms. A larger ISF area (i.e. larger super cell cross-sectional area) would reduce the standard deviation while leaving the mean value almost unchanged [26]. Most importantly, as will be discussed next, not all of these local configurations correspond to stable fcc phases, and thus, the values of $\gamma_{\rm isf}$ and $\gamma_{\rm usf}$ associated with them would not be very meaningful.

Based on the present DFT calculations, 31 of the 90 slip planes have a positive γ_{isf} , for which the ISF corresponds locally to HCP stacking, and the remaining ones have a negative

 $\gamma_{\rm isf}$. Similar to a prior DFT work in NiFe [45], we found that full structural relaxation only alters the values of $\gamma_{\rm isf}$ slightly. The sign of $\gamma_{\rm isf}$ may be an indication of the stability of the fcc phase with respect to the HCP phase. To the first order, the axial next-nearest neighbor Ising model [46] expresses

$$\gamma_{\rm isf} = \frac{2(E_0^{\rm hcp} - E_0^{\rm fcc})}{A_0^{\rm fcc}},\tag{13}$$

where $E_0^{\rm hcp}$ and $E_0^{\rm fcc}$ are the free energy for the full relaxed HCP and fcc structures, respectively, and $A_0^{\rm fcc}$ is the fcc atomic area on the fault plane. It has been shown in prior DFT simulations (for six component MPEAs, RhIrPdPtNiCu [41]) that the ISF energies calculated directly by equation (4) and approximated by equation (13) differ by less than 20 mJ m⁻². Accordingly, a negative $\gamma_{\rm isf}$ we calculate here is a good indication that the HCP phase is more stable than the fcc phase in some configurations [47] and the 31 GSFE surfaces with positive $\gamma_{\rm isf}$ can be related to dislocations in an fcc lattice.

For subsequent dislocation core simulations, the DFT GSFE calculations are used to parameterize the entire GSFE surface for the (111) plane in the likely fcc phase configurations. Figure 5(a) presents the entire GSFE surface based on the Fourier series function for one configuration. Comparing the GSFE surface to the one calculated in full by DFT, we observe that it provides a good representation of all the maxima and minima appearing in the surface. This case, like the others, exhibits a GSFE surface bearing energy level variations that are consistent with that of a pure fcc metal.

To analyze the energy level variations in more detail, figure 6 displays the GSFE curves along the $\langle 112 \rangle$ and $\langle 110 \rangle$ directions for eight of the fcc configurations. The $\langle 112 \rangle$ direction is aligned with the partial dislocation Burgers vector and so for all fcc, this GSFE curve contains the local minimum at $\gamma_{\rm isf}$ and local maximum at $\gamma_{\rm usf}$. For all pure fcc metals, the local minimum $\gamma_{\rm isf}$ is achieved at $d_x = d_{x0}/3$ corresponding to the value of the Shockley partial dislocations. The eight MPEA configurations discussed here are seen to exhibit a local minimum also at this shift vector. Two important local maxima are $\gamma_{\rm usf}$ at $d_x = d_{x0}/6$ in the $\langle 112 \rangle$ curve, and at $d_z = d_{z0}/2$ in the $\langle 110 \rangle$ curve. Some configurations exhibit a local maximum $\gamma_{\rm usf}$ at $d_x \approx 0.19 d_{x0}$. This anomaly is not unusual and is also seen in DFT calculated curves for Al and Pt [21].

For some cases, $\gamma_{\rm usf}$ is not a maximum but lies in a shallow minimum at $d_z = d_{z0}/2$, such as one slip plane in configuration 112323, a feature that is uncharacteristic of pure fcc metals. These GSFE curves were generated from the Fourier series function informed by 11 DFT-calculated points (see equation (5) and figure 5(b)). For this case, direct DFT calculations for the entire $\langle 110 \rangle$ GSFE curve are conducted, and this result is included for comparison in figure 6. The direct DFT calculations show a local maximum at the same d_z , indicating that the shallow local minimum produced in the Fourier series function approximation is an artifact. Since any local minima in the $\langle 110 \rangle$ GSFE curves are still much higher than the corresponding $\gamma_{\rm isf}$, they lie along a path not favored by the dislocation, and it is unlikely they will affect the dislocation dissociation.

Last, direct DFT calculations treating the material as a magnetic structures are also conducted to validate the assumption that magnetic effects are small. The comparison is presented in figure 6 with the solid square symbols corresponding to the calculations taking magnetism into account. For selected cases with negative $\gamma_{\rm isf}$, we repeated DFT calculations with magnetism and found that $\gamma_{\rm isf}$ remained negative. However, caution is needed that the magnetism may be important in other MPEAs containing Cr, Co, Fe, or Ni [48]. In some

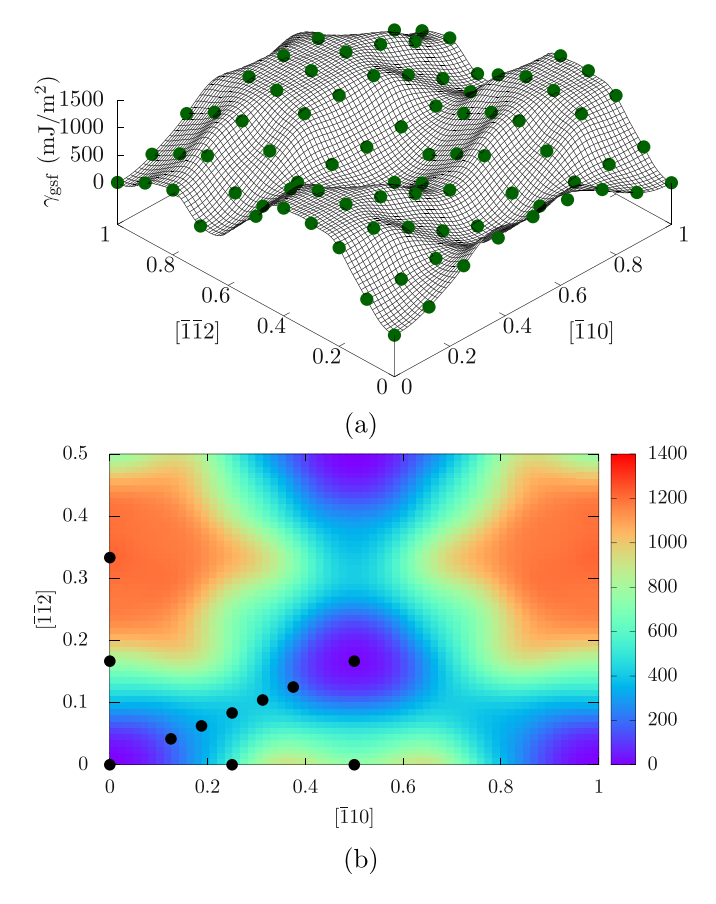


Figure 5. (a) 3D relaxed GSFE surface on one of the (111) planes in configuration 112323 along both [$\bar{1}\bar{1}2$] and [$\bar{1}10$] directions. Results based on direct DFT calculations on non-magnetic structures are shown as dark green spheres. (b) Is the projection of (a) onto the (111) plane. $\gamma_{\rm isf}=16.22~{\rm mJ~m^{-2}}$ and $\gamma_{\rm usf}=417.71~{\rm mJ~m^{-2}}$. The 11 points for the Fourier series representation (equation (5)) are highlighted by black filled circles.

cases, it is challenging to predict correct results by DFT even when the magnetism is considered [49].

4. PFDD simulations

To estimate the structures of dislocation in equal-molar fcc CoNiRu MPEAs, we employ the PFDD method [24]. The widths spanned by dislocation cores in fcc are usually too large to be calculated by DFT alone, apart from a few exceptions, like Al, which have small core widths [50, 51]. However, DFT calculations for the lattice parameter, stiffness tensor, and GSFE surfaces pertaining to each configuration corresponding to an fcc crystal can be used as input into the PFDD model. Among all 90 cases studied, eight distinct cases have calculable elastic constants and are associated with the fcc crystal. Before presenting the dislocation core results, we first briefly introduce the PFDD method as it is applied to MPEAs and then describe the simulation set-up for the screw and edge dislocations.

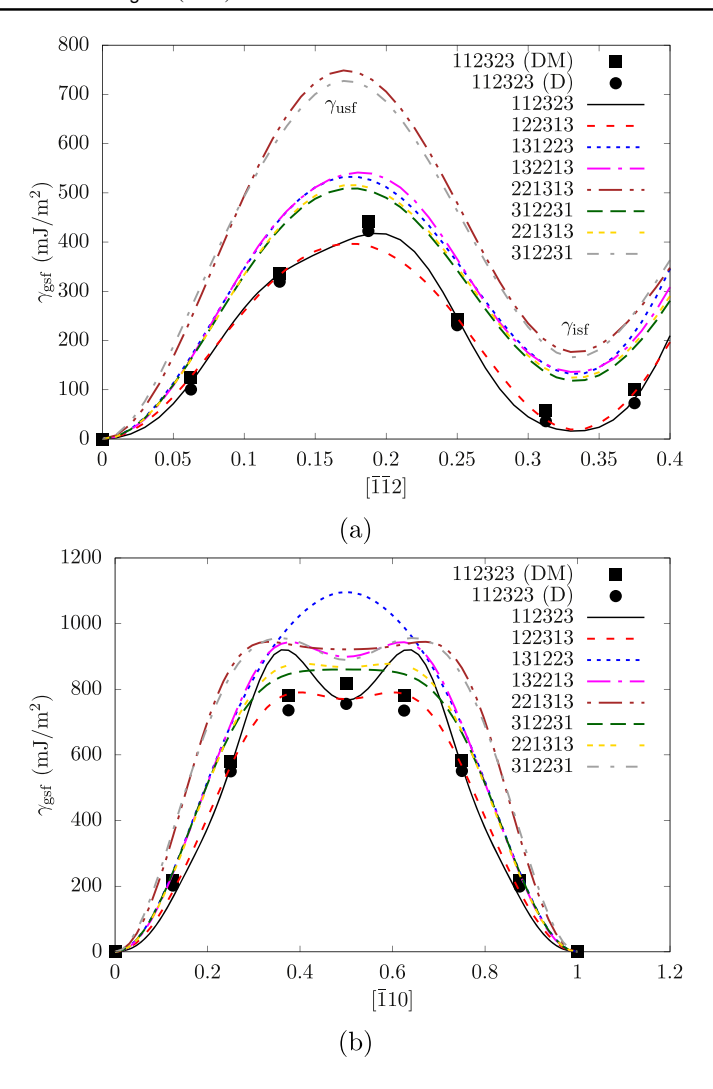


Figure 6. 11-term Fourier series function-based GSFE curves along the $\langle 112 \rangle$ and $\langle 110 \rangle$ directions for 8 cases whose stiffness tensors \mathbf{C}_{E} are calculable and ISF energies γ_{isf} are positive. All curves are informed by DFT calculations on non-magnetic structures. For one case (112323), results based on direct DFT calculations on non-magnetic structures (D) and those on magnetic structures (DM) are shown for comparison.

4.1. PFDD formulation

In a PF dislocation model, an order parameter ϕ_{α} represents the state of slip for the α th slip system, with $\phi_{\alpha}=0$ and 1 corresponding to the unslipped and slipped states, respectively. Let \boldsymbol{u} represent the displacement field, $\boldsymbol{H}=\nabla\boldsymbol{u}$ the distortion field, and $\boldsymbol{E}=(\boldsymbol{H}+\boldsymbol{H}^{\mathrm{T}})/2$ the strain field. For fcc materials, the total free energy density of a dislocated system ψ is the sum of the elastic energy density ψ_{ela} , the GSFE density ψ_{gsf} , and the gradient energy density ψ_{gra} [52], i.e.

$$\psi(\mathbf{E}, \, \boldsymbol{\phi}, \, \nabla \boldsymbol{\phi}) = \psi_{\text{ela}}(\mathbf{E}, \, \boldsymbol{\phi}) + \psi_{\text{gsf}}(\boldsymbol{\phi}) + \psi_{\text{gra}}(\nabla \boldsymbol{\phi}). \tag{14}$$

In particular

$$\psi_{\text{ela}}(E, \phi) = \frac{1}{2}(E - E_{\text{R}}(\phi)) \cdot \mathbf{C}_{\text{E}}(E - E_{\text{R}}(\phi)), \tag{15}$$

$$\psi_{\rm gsf}(\phi) = \frac{\gamma_{\rm gsf}(\phi)}{l_{\rm gsf}},\tag{16}$$

$$\psi_{\text{gra}}(\nabla \phi) = \sum_{\alpha,\beta=1}^{n} \eta_{g0}^{\alpha\beta} \nabla \phi_{\alpha} \cdot N_{\alpha\beta} \nabla \phi_{\beta}, \tag{17}$$

where n is the total number of order parameters, $E_R = (H_R + H_R^T)/2$ is the residual strain, $l_{\rm gsf}$ is the interplanar spacing between two adjacent slip planes based on which $\gamma_{\rm gsf}$ is calculated, and $\eta_{s0}^{\alpha\beta}$ are the gradient energy coefficients, and

$$\boldsymbol{H}_{\mathrm{R}}(\phi) = \sum_{\alpha=1}^{n} \frac{b_{\alpha} \phi_{\alpha}}{d_{\alpha}} \, \boldsymbol{s}_{\alpha} \otimes \boldsymbol{n}_{\alpha}, \tag{18}$$

$$N_{\alpha\beta} = \frac{\boldsymbol{b}_{\alpha} \cdot \boldsymbol{b}_{\beta}}{d_{\alpha}d_{\beta}} [(\boldsymbol{n}_{\alpha} \cdot \boldsymbol{n}_{\beta})\boldsymbol{I} - \boldsymbol{n}_{\beta} \otimes \boldsymbol{n}_{\alpha}], \tag{19}$$

where s_{α} is the slip direction, n_{α} is the slip plane unit normal, $b_{\alpha} = b_{\alpha} s_{\alpha}$ is the slip vector, and d_{α} is the interplanar spacing between two adjacent slip planes, of the α th order parameter. In the current work of a single slip plane, n=3 and $l_{\rm gsf}=d_{\alpha}=d_{\beta}=d_{111}$, where $d_{111}=a_0/\sqrt{3}$ is the interplanar distance between two adjacent {111} planes.

The time-dependent Ginzburg–Landau equation is employed to recursively minimize the system free energy with respect to each ϕ_{α} , i.e.

$$\dot{\phi}_{o} = m_0 [\nabla \cdot \partial_{\nabla \phi_{o}} \psi_{\text{ora}} - \partial_{\phi_{o}} (\psi_{\text{ela}} + \psi_{\text{osf}})], \tag{20}$$

where the superposed dot denotes the time derivative and m_0 is the Ginzburg-Landau coefficient.

4.2. Simulation set-up

The 3D periodic simulation cell used in PFDD simulations consists of a dipole of two dislocations of the same type but with oppositely signed Burgers vectors. L_x , L_y , and L_z are the edge length of the cell along the x, y, and z directions, respectively. The two dislocation lines lie along the y direction on the mid-z plane and are separated by $L_x/2$ along the x direction. In the case of a pure edge dislocation dipole, the crystallographic orientations are $x[1\bar{1}0]$, $y[11\bar{2}]$, and z[111]. For the pure screw dislocation dipole, they are $x[11\bar{2}]$, $y[\bar{1}10]$, and z[111]. In what follows, let $b = a_0/\sqrt{2}$ be the magnitude of the Burgers vector of one dislocation.

The simulations are performed for the top eight slip planes listed in table 2, with their individual lattice parameter a_0 , anisotropic stiffness tensor \mathbf{C}_E , and GSFE surface, as calculated by DFT. To determine the energetically favorable dislocation core structure, the total energy of these dislocated systems is minimized according to equation (20). For this process, we set m_0 equal to unity, the timestep size as 0.02, and enforce that all slips be confined to the slip plane [53]. For all configurations studied, energy minimization leads to the dissociation of these dislocations into two Shockley partials that glide apart on the mid-z plane. Iterations are terminated when the Euclidean norm of the difference in global vector of each order parameter between successive iterations is smaller than 10^{-4} .

Table 3. Material parameters for Ni based on an EAM potential [59], experiments [60, 61], and DFT [21]: lattice parameter a_0 (in Å), elastic constants C_{11} , C_{12} , C_{44} (in GPa), ISF energy γ_{isf} (in mJ m⁻²), and USF energy γ_{usf} (in mJ m⁻²).

	a_0	C_{11}	C_{12}	C_{44}	$\gamma_{ m isf}$	$\gamma_{ m usf}$
EAM	3.52	240.6	150.3	119.2	128.9	257.1
Exp [60]	3.524	247	153	122		
Exp [61]					120-130	
DFT	3.52	271.5	157.1	128.1	144.5	289

Several calculations were performed to ensure that the periodic cell size and in-plane grid spacings are, respectively, large enough and small enough to minimize numerical size effects. Particularly for the grid spacing, prior GPN models found that, within the slip plane, 3 or 4 grid points per Burgers vector were sufficient to achieve numerical convergence [54, 55]. Our own convergence study, which will be discussed later, shows that all PFDD simulations can be carried out reliably using a uniform in-plane grid spacing of $0.25d_{111}$ and 256 grid points in each direction. Along the slip plane normal, we choose a uniform grid spacing of d_{111} [56].

To identify the extent of the relaxed dislocation core structures, the disregistry fields produced by the dislocations are analyzed. The disregistry field ζ , is a continuous vector field that represents the discrete atomic displacements caused by a dislocation [36]. The component of ζ along the β direction, ζ_{β} , is

$$\zeta_{\beta} = \sum_{\alpha=1}^{n} \phi_{\alpha} \, \boldsymbol{b}_{\alpha} \cdot \boldsymbol{s}_{\beta}, \tag{21}$$

where $\beta = 1$ and $\beta = 2$ represent the directions along and normal to the full dislocation Burgers vector, respectively. It follows that the center of each Shockley partial dislocation is determined by projecting the disregistry field onto the partial dislocation direction [36]. The ISF width d is then measured as the distance between the centers of two partial dislocations.

4.3. Determination of the gradient energy coefficients $\eta_{00}^{\alpha\beta}$

An important component of the total energy density in the PFDD formulation is the gradient energy density $\psi_{\rm gra}$. The effects of $\psi_{\rm gra}$ on dislocation cores will be explored in this work. Prior PF-based simulations in Al and Au [36, 52, 57] showed that the predicted dislocation core structures are in better agreement with MS when $\psi_{\rm gra}$ is included. This term introduces material dependent coefficients $\eta_{g0}^{\alpha\beta}$ for which there is no standard number of coefficients that may be used or a method for quantifying them. Here, for simplicity, a uniform $\eta_{g0}^{\alpha\beta}$ is used for all sets of $\alpha\beta$ for each dislocation type. Regarding characterization, in GPN modeling of pure-type dislocations in Ag, Al, and Cu, $\eta_{g0}^{\alpha\beta}$ were determined by fitting the GPN-based disregistry profiles to MS-based ones [58]. Applying the same approach here would ideally entail characterizing $\eta_{g0}^{\alpha\beta}$ by fitting the PFDD-based disregistry profile to that from DFT. However, DFT calculations of dislocations in either pure metals or MPEAs are computationally expensive. On the other hand, there exists no appropriate interatomic potential for the CoNiRu ternary system, to the best of our knowledge. To approximate a value for $\eta_{g0}^{\alpha\beta}$, we select pure Ni as a surrogate for the fcc CoNiRu MPEA and compare PFDD disregistry profiles with MS calculated ones for pure screw and edge dislocations.

For pure Ni in MS, we use the embedded-atom method (EAM) potential of Foiles and Hoyt [59]. Table 3 provides the material parameters predicted by this potential, including the

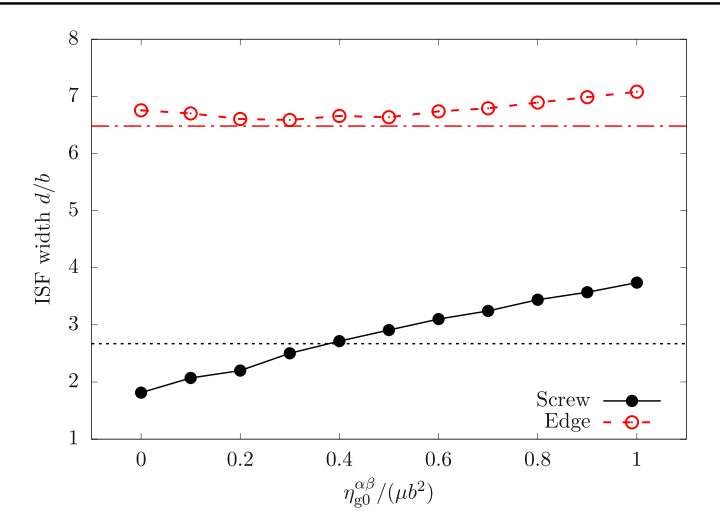


Figure 7. ISF widths, d, predicted by PFDD, for the screw and edge dislocations in Ni, with respect to the gradient energy coefficient $\eta_{\rm g0}^{\alpha\beta}$. When $\eta_{\rm g0}^{\alpha\beta}=0$, PFDD simulations are without the gradient energy density $\psi_{\rm gra}$. MS-based d values are shown as horizontal dashed lines, with the top and bottom ones for the edge (6.48b) and screw (2.67b) dislocations, respectively.

Table 4. Edge lengths L_x , L_y , and L_z of the MS simulation cells (in Å), the corresponding number of atoms N_{atom} , and ISF width d (in b), for screw and edge dislocations.

 L_x L_y	L_z	$N_{ m atom}$	d
 		843 648 554 400	

lattice parameter a_0 , elastic constants C_{11} , C_{12} , C_{44} , ISF energy $\gamma_{\rm isf}$, and USF energy $\gamma_{\rm usf}$. These values are found to be in good agreement with experimental [60, 61] and DFT [21] data. MS simulations are carried out by LAMMPS [62]. The simulation set-up is similar to that described in section 4.2, with the edge lengths of the simulation cell and numbers of atoms involved summarized in table 4. In each simulation, an undissociated, perfect dislocation dipole is first created by applying the corresponding isotropic elastic displacement field to all atoms. The dislocated system is then relaxed using the conjugate gradient method. The relaxation step is terminated when one of the following two criteria is satisfied: (i) the change in energy between successive iterations divided by the most recent energy magnitude is less than or equal to 10^{-15} or (ii) the length of the global force vector for all atoms is less than or equal to 10^{-15} eV Å⁻¹. As defined earlier, from the disregistry profile, the ISF width can be determined, which is d = 2.67b and 6.48b for a screw or an edge dislocation, respectively.

For this characterization step, PFDD simulations in Ni are carried out, with lattice parameter a_0 , stiffness tensor $\mathbf{C}_{\rm E}$, and GSFE surface $\gamma_{\rm gsf}$ informed by the same EAM potential. Different $\eta_{\rm g0}^{\alpha\beta}$, ranging from 0 to μb^2 , in increments of $0.1\mu b^2$, are considered. For each value, the disregistry profiles and ISF widths d are obtained and directly compared to those from MS. Figure 7 shows the variation in d with $\eta_{\rm g0}^{\alpha\beta}$ for both screw and

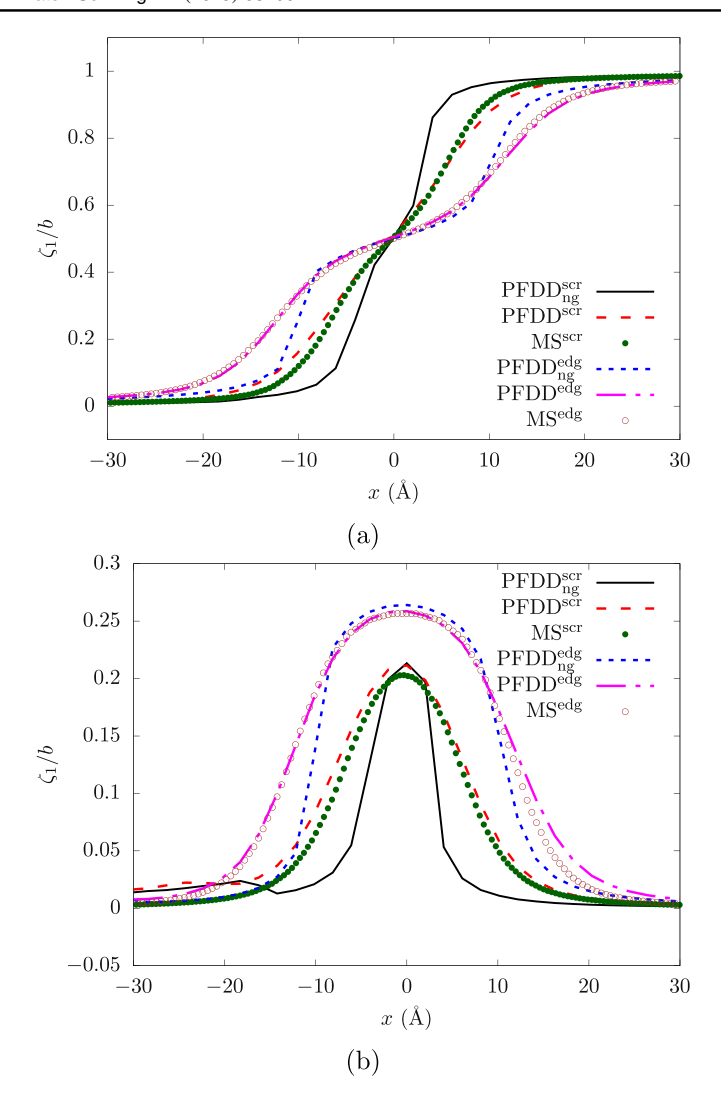


Figure 8. PFDD-predicted disregistry fields of screw and edge dislocations in Ni (a) along and (b) normal to the perfect dislocation Burgers vector direction. The subscript 'ng' denotes the results for which the gradient energy density $\psi_{\rm gra}$ is not included in the system free energy. When $\psi_{\rm gra}$ is included, $\eta_{\rm g0}^{\alpha\beta}=0.38\mu b^2$ and $0.3\mu b^2$ for the screw and edge dislocation, respectively. MS results with the same EAM potential [59] are also shown for comparison.

edge dislocations. The values of $\eta_{g0}^{\alpha\beta}$ providing the best agreement are $0.38\mu b^2$ and $0.3\mu b^2$ for the screw and edge dislocations, respectively. Hence, for subsequent PFDD calculations of the dislocation core structures in CoNiRu MPEAs, these two values of $\eta_{g0}^{\alpha\beta}$ will be adopted.

Figure 8 presents the PFDD disregistry profiles corresponding to the use of these two values of $\eta_{g0}^{\alpha\beta}$, as well as those without the gradient energy in the system free energy, i.e. $\eta_{g0}^{\alpha\beta}=0$. Neglecting the gradient energy term clearly leads to poor agreement for Ni.

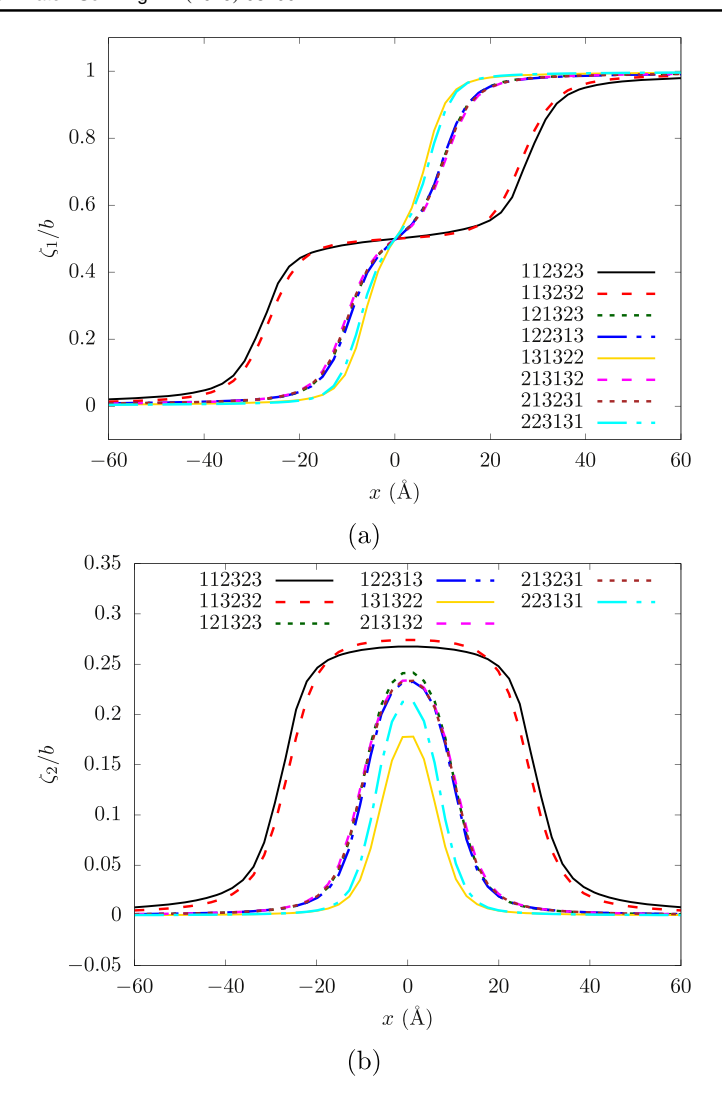


Figure 9. PFDD-predicted disregistry fields of a screw dislocation in eight configurations in equal-molar CoNiRu MPEAs (a) along and (b) normal to the perfect dislocation Burgers vector direction.

4.4. Dislocation core structures

Figures 9 and 10 present the calculated disregistry fields for the screw and edge dislocations, respectively, for eight different atomic configurations. In all cases, the dislocation splits into two partials with equal valued Burgers vectors. This consistency can be explained by the fact that the local minimum in the $\langle 112 \rangle$ GSFE curve occurs at a displacement shift of $d_{x0}/3$.

The outstanding result is the variation in area spanned by the dislocation cores among these eight configurations. Some configurations span over 6 nm while some others less than 1 nm. Using '|' to indicate the slip plane, we note that two slip planes (13|1322 and 2231|31) provide the narrowest ISFs and two others (1123|23 and 1132|32) provide the widest ISFs for the same type of dislocation. These cases can be related to the particular atoms that straddle

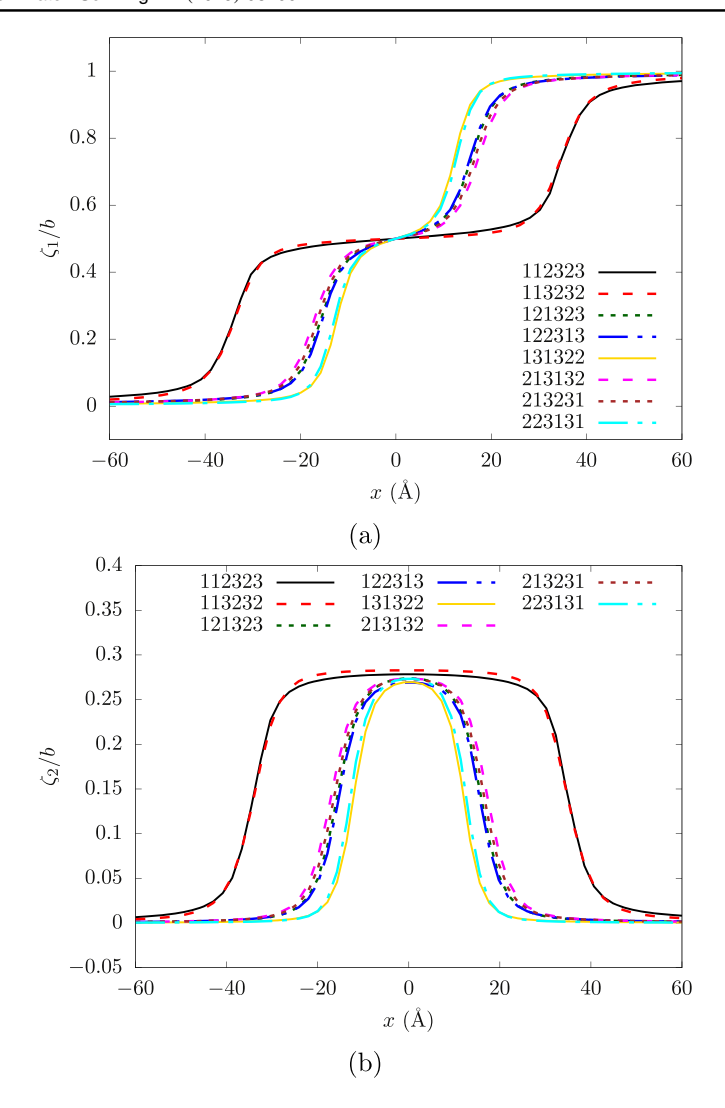


Figure 10. PFDD-predicted disregistry fields of an edge dislocation in eight configurations in equal-molar CoNiRu MPEAs (a) along and (b) normal to the perfect dislocation Burgers vector direction.

the glide plane. The value at the local minimum $\gamma_{\rm isf}$ results from the change in the charge redistribution as the atoms are displaced and change in nearest atomic neighbors. Evidently, we find that some pairs of atomic elements produce much larger (or smaller) changes as atoms on both sides of the glide plane. Our DFT results show that the narrowest ISFs are associated with only Co and Ru atoms across the faulted plane, leading to a relatively high $\gamma_{\rm isf}$ of about 170 mJ m⁻². In contrast, the widest ISFs have only Ni and Ru atoms on this plane, and a relatively low $\gamma_{\rm isf}$ of about 17 mJ m⁻².

Figure 11 presents the variation in the ISF width d for screw and edge dislocations for eight cases with respect to $\gamma_{\rm isf}/(\mu b)$. It is found that the in-plane grid spacing $0.25d_{111}$ used in this work is indeed sufficiently small. In addition, the ISF widths d of the edge dislocation are consistently larger than those of the screw dislocation, provided they lie within the same slip

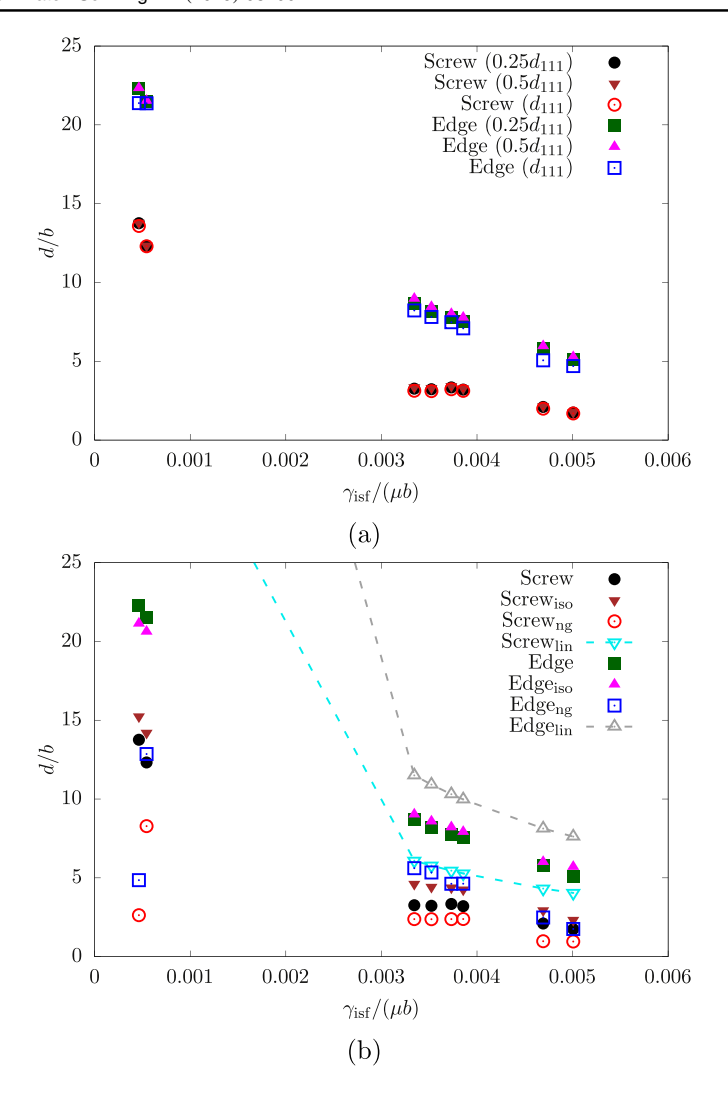


Figure 11. ISF widths, d, predicted by PFDD, for the 8 screw and edge dislocations considered in equal-molar CoNiRu MPEAs. In (a), results based on three grid spacings $(d_{111}, 0.5d_{111})$, and $0.25d_{111}$) are compared. In (b), the subscripts 'iso', 'ng', and 'lin', respectively, denote the PFDD results for which an isotropic stiffness tensor C_E is used, the PFDD results for which the gradient energy density $\psi_{\rm gra}$ is not included in the system free energy, and the isotropic linear elasticity predictions based on equations (1) and (2). For the two smallest $\gamma_{\rm isf}/(\mu b)$, linear elasticity predicts 37.697b and 44.202b for the screw dislocation, and 72.318b and 84.817b for the edge dislocation.

plane in the same atomic configuration. The general screw/edge dependence observed here is no different than that expected for dislocations in a pure fcc metal and is similar for all configurations, indicating that it is an outcome of the elastic interaction and not the local atomic bonding across the plane.

Among the eight cases, $\gamma_{\rm isf}/(\mu b)$ ranges from 0.0004 to 0.005. The lower $\gamma_{\rm isf}/(\mu b)$, the more extended the dislocation. The trend would be expected, since the other parameters influencing the dislocation core size, a_0 and C_E , do not vary substantially (figure 2 and

table 2) in comparison with $\gamma_{\rm isf}$. Our results show a significant dispersion in the ISF width d, changing by a factor of 7.17 and 3.06 for screw and edge dislocations, respectively. The distribution is particularly wide for the screw dislocation and would suggest that if the local ordering were to vary spatially over nanometer-sized regions, screw dislocations may develop kinks along the line.

Based on γ_{isf} , analytical models (equations (1) and (2)) ought to provide a reasonable estimate. Yet, we find that the difference between the PFDD calculations and the analytical model for d increases as γ_{isf} decreases, with the latter model overestimating d. For instance when $\gamma_{isf}/(\mu b) = 0.005$, a large value, PFDD predicts 0.602 and 1.959 nm for the screw and edge dislocations, respectively, compared to 1.033 nm and 1.945 nm from the analytic model. The difference is much larger for two configurations 112323 and 122313 for which $\gamma_{\rm isf}/(\mu b) \approx 0.0004$, a much lower value, wherein the PFDD results are 4.322 and 2.262 nm for the screw and edge dislocations, respectively, while the analytical model yields 11.283 and 21.651 nm. We remark that, because the two configurations have a relatively large isotropic shear modulus μ and relatively small ISF energy γ_{isf} , the normalized ISF energies, $\gamma_{\rm isf}/(\mu b)$, are small. Indeed, the values of $\gamma_{\rm isf}/(\mu b)$, ~ 0.0004 , are smaller than any fcc pure metal, e.g. Ag and Cu, for which $\gamma_{isf}/(\mu b) \approx 0.002$ [21]. Therefore, the two smallest values of $\gamma_{isf}/(\mu b)$ analyzed here are beyond those explored in some previous GPN/PF work [20, 21, 23, 36] which only considered fcc pure metals. The large deviation between the analytical models and PFDD calculations is unknown and is likely not solely due to the small values of $\gamma_{\rm isf}/(\mu b)$. We confirm that it is not caused by (i) simulation cell size, (ii) grid spacing, or (iii) spurious GSFE surfaces. Validation, however, would be best performed against experimental data. Unfortunately experiments on an MPEA of similar but not the same chemical composition show widely faults and twins and is not quantitative.

To examine the effect of elastic anisotropy in isolation, the same simulations are repeated with $\psi_{\rm gra}$ included but with isotropic ${\bf C}_{\rm E}$ in Voigt form. This set of results is designated by subscript 'iso'. Under the assumption of isotropic elasticity, elastic interactions develop between dislocations of like character. With increasing degree of elastic anisotropy (increasing $A_{\rm c}$ from unity), the elastic interactions between the screw and edge components of the dislocation grow [12]. PFDD calculations find that the effect of elastic anisotropy is to decrease the ISF width relative to that of isotropic ISF width for the screw dislocation and to increase it for the edge dislocation. The difference is, however, small, causing an approximately average 10% change. The minute influence is a consequence of the low anisotropy index (<1.5) of this MPEA. A recent study employing the GPN model reported the same trend for a broad range of pure fcc metals and further put forth an analytic model predicting that the ratios in d scale with $A_{\rm c}$ [23].

To isolate the effect of the gradient energy density $\psi_{\rm gra}$, the same simulations are repeated with anisotropic ${\bf C}_{\rm E}$ but without $\psi_{\rm gra}$. This set of calculations is designated by subscript 'ng'. We find that introducing $\psi_{\rm gra}$ to the system free energy increases d. Evidently it is more energetically favorable for the dislocation to reduce the interaction energy between the partial dislocations by increasing d than to reduce the energetic penalty associated with increasing the fault area.

5. Conclusions

In this paper, we use *ab initio*-informed PF modeling method to study static dislocation core structures in equal-molar CoNiRu MPEAs. By exhausting all possible configurations/slip planes in a small super cell containing six atoms in equal-molar CoNiRu MPEAs, our results

show small variations in lattice parameter a_0 and stiffness tensor $\mathbf{C}_{\rm E}$, low to medium elastic anisotropy index $A_{\rm c}$, and large variations in GSFE surfaces $\gamma_{\rm gsf}$. For the same type of dislocation in the fcc lattice, our results reveal a large variation in dislocation core structures and ISF widths. For the range of $\gamma_{\rm isf}/(\mu b)$ calculated for the fcc MPEA, 0.0004 to 0.005, we show that the ISF widths vary by a factor of 7.17 and 3.06 for screw and edge dislocations, respectively.

In modeling dislocation dynamics within strained crystals using this model, at least for this specific MPEA, it would be reasonable to adopt a constant a_0 and \mathbf{C}_E everywhere, while spatially varying $\gamma_{\rm gsf}$. Further, we find that this material is nearly isotropic, such that assuming elastic isotropy in the calculation is reasonable. Yet MPEAs, in general, may not be assumed as elastic isotropic, as in previous mesoscale modeling work [17, 18].

For many of the configurations, we find that the GSFE surfaces possessed negative ISFE $\gamma_{\rm isf}$, suggesting that the HCP phase is more stable than the fcc phase. While only dislocations in fcc phase are analyzed in this work, the present *ab initio*-informed PF modeling framework can be readily applied to dislocations in HCP lattice with the recommendation that the GSFE surfaces for targeted glide planes (e.g. basal, prismatic, pyramidal) are informed by DFT.

Acknowledgments

We thank Dr Marie-Agathe Charpagne, Dr Venkata Vamsi Koruprolu, and Ms Lauren Smith for helpful discussions. The authors gratefully acknowledge support from the Office of Naval Research under contract ONR BRC Grant N00014-18-1-2392. The work of SX was supported in part by the Elings Prize Fellowship in Science offered by the California Nano-Systems Institute on the UC Santa Barbara campus. Use was made of computational facilities purchased with funds from the National Science Foundation (CNS-1725797) and administered by the Center for Scientific Computing (CSC). The CSC is supported by the California NanoSystems Institute and the Materials Research Science and Engineering Center (MRSEC; NSF DMR 1720256) at UC Santa Barbara. This work used the Extreme Science and Engineering Discovery Environment (XSEDE), which is supported by National Science Foundation Grant Number ACI-1053575.

ORCID iDs

Yanqing Su https://orcid.org/0000-0003-0790-5905 Shuozhi Xu https://orcid.org/0000-0003-0121-9445

References

- [1] Yeh J-W, Chen S-K, Lin S-J, Gan J-Y, Chin T-S, Shun T-T, Tsau C-H and Chang S-Y 2004 Nanostructured high-entropy alloys with multiple principal elements: novel alloy design concepts and outcomes *Adv. Eng. Mater.* **6** 299–303
- [2] Cantor B, Chang I T H, Knight P and Vincent A J B 2004 Microstructural development in equiatomic multicomponent alloys *Mater. Sci. Eng.* A 375-377 213-8
- [3] Miracle D B and Senkov O N 2017 A critical review of high entropy alloys and related concepts Acta Mater. 122 448–511
- [4] Diao H Y, Feng R, Dahmen K A and Liaw P K 2017 Fundamental deformation behavior in highentropy alloys: an overview Curr. Opin. Solid State Mater. Sci. 21 252–66
- [5] Singh P, Smirnov A V and Johnson D D 2015 Atomic short-range order and incipient long-range order in high-entropy alloys *Phys. Rev.* B 91 224204

- [6] Owen L R and Jones N G 2018 Lattice distortions in high-entropy alloys J. Mater. Res. 33
- [7] Lee C et al 2018 Lattice distortion in a strong and ductile refractory high-entropy alloy Acta Mater. 160 158–72
- [8] Smith T M, Hooshmand M S, Esser B D, Otto F, McComb D W, George E P, Ghazisaeidi M and Mills M J 2016 Atomic-scale characterization and modeling of 60° dislocations in a highentropy alloy Acta Mater. 110 352–63
- [9] Gludovatz B, Hohenwarter A, Thurston K V S, Bei H, Wu Z, George E P and Ritchie R O 2016 Exceptional damage-tolerance of a medium-entropy alloy CrCoNi at cryogenic temperatures Nat. Commun. 7 10602
- [10] Liang Y-J et al 2018 High-content ductile coherent nanoprecipitates achieve ultrastrong high-entropy alloys Nat. Commun. 9 4063
- [11] Xu S, Rigelesaiyin J, Xiong L, Chen Y and McDowell D L 2018 Generalized continua concepts in coarse-graining atomistic simulations Generalized Models and Non-classical Approaches in Complex Materials 2 (Advanced Structured Materials) (Cham: Springer) pp 237–60
- [12] Hull D and Bacon D J 2011 Introduction to Dislocations 5th edn (Oxford: Butterworth-Heinemann)
- [13] Varvenne C, Luque A and Curtin W A 2016 Theory of strengthening in fcc high entropy alloys Acta Mater. 118 164–76
- [14] Wang P, Wu Y, Liu J and Wang H 2017 Impacts of atomic scale lattice distortion on dislocation activity in high-entropy alloys Extrem. Mech. Lett. 17 38–42
- [15] Wang Z, Baker I, Cai Z, Chen S, Poplawsky J D and Guo W 2016 The effect of interstitial carbon on the mechanical properties and dislocation substructure evolution in Fe_{40.4}Ni_{11.3}Mn_{34.8}Al_{7.5}Cr₆ high entropy alloys *Acta Mater.* 120 228–39
- [16] Rao S I, Woodward C, Parthasarathy T A and Senkov O 2017 Atomistic simulations of dislocation behavior in a model fcc multicomponent concentrated solid solution alloy *Acta Mater.* 134 188–04
- [17] Zeng Y, Cai X and Koslowski M 2019 Effects of the stacking fault energy fluctuations on the strengthening of alloys Acta Mater. 164 1–11
- [18] Zhang L, Xiang Y, Han J and Srolovitz D J 2019 The effect of randomness on the strength of highentropy alloys Acta Mater. 166 424–34
- [19] Schoeck G 2006 The core structure of dislocations: Peierls model versus atomic simulation Acta Mater. 54 4865–70
- [20] Hunter A, Zhang R F, Beyerlein I J, Germann T C and Koslowski M 2013 Dependence of equilibrium stacking fault width in fcc metals on the γ-surface Modelling Simul. Mater. Sci. Eng. 21 025015
- [21] Hunter A, Zhang R F and Beyerlein I J 2014 The core structure of dislocations and their relationship to the material γ -surface J. Appl. Phys. 115 134314
- [22] Vitek V 1992 Structure of dislocation cores in metallic materials and its impact on their plastic behaviour *Prog. Mater. Sci.* 36 1–27
- [23] Szajewski B A, Hunter A, Luscher D J and Beyerlein I J 2018 The influence of anisotropy on the core structure of Shockley partial dislocations within fcc materials *Modelling Simul. Mater. Sci.* Eng. 26 015010
- [24] Hunter A, Beyerlein I J, Germann T C and Koslowski M 2011 Influence of the stacking fault energy surface on partial dislocations in fcc metals with a three dimensional phase field dynamics model *Phys. Rev.* B 84 144108
- [25] Ding J, Yu Q, Asta M and Ritchie R O 2018 Tunable stacking fault energies by tailoring local chemical order in CrCoNi medium-entropy alloys *Proc. Natl Acad. Sci. USA* 115 8919–24
- [26] Zhao S, Osetsky Y, Stocks G M and Zhang Y 2019 Local-environment dependence of stacking fault energies in concentrated solid-solution alloys npj Comput. Mater. 5 13
- [27] Kresse G and Furthmüller J 1996 Efficient iterative schemes for ab initio total-energy calculations using a plane-wave basis set *Phys. Rev.* B 54 11169–86
- [28] Blöchl P E 1994 Projector augmented-wave method *Phys. Rev.* B **50** 17953–79
- [29] Kresse G and Joubert D 1999 From ultrasoft pseudopotentials to the projector augmented-wave method Phys. Rev. B 59 1758–75
- [30] Perdew J P, Burke K and Ernzerhof M 1996 Generalized gradient approximation made simple Phys. Rev. Lett. 77 3865–8

- [31] Methfessel M and Paxton A T 1989 High-precision sampling for Brillouin-zone integration in metals Phys. Rev. B 40 3616–21
- [32] Huang S, Li W, Lu S, Tian F, Shen J, Holmstrm E and Vitos L 2015 Temperature dependent stacking fault energy of FeCrCoNiMn high entropy alloy Scr. Mater. 108 44–7
- [33] Monkhorst H J and Pack J D 1976 Special points for Brillouin-zone integrations Phys. Rev. B 13 5188–92
- [34] Zhang S H and Zhang R F 2017 AELAS: automatic ELAStic property derivations via high-throughput first-principles computation Comput. Phys. Commun. 220 403–16
- [35] Lu G, Kioussis N, Bulatov V V and Kaxiras E 2000 Generalized-stacking-fault energy surface and dislocation properties of aluminum *Phys. Rev.* B 62 3099–108
- [36] Xu S, Mianroodi J R, Hunter A, Beyerlein I J and Svendsen B 2019 Phase-field-based calculations of the disregistry fields of static extended dislocations in fcc metals *Phil. Mag.* 99 1400–28
- [37] Schoeck G 2001 The core structure, recombination energy and Peierls energy for dislocations in Al Phil. Mag. A 81 1161–76
- [38] Zhao Y Y, Lei Z F, Lu Z P, Huang J C and Nieh T G 2019 A simplified model connecting lattice distortion with friction stress of Nb-based equiatomic high-entropy alloys *Mater. Res. Lett.* 7 340–6
- [39] Zunger A, Wei S-H, Ferreira L G and Bernard J E 1990 Special quasirandom structures Phys. Rev. Lett. 65 353–6
- [40] van de Walle A, Tiwary P, de Jong M, Olmsted D L, Asta M, Dick A, Shin D, Wang Y, Chen L Q and Liu Z K 2013 Efficient stochastic generation of special quasirandom structures Calphad 42 13–8
- [41] Yin B and Curtin W A 2019 First-principles-based prediction of yield strength in the RhIrPdPtNiCu high-entropy alloy *npj Comput. Mater.* 5 14
- [42] Kim D E, Shang S L and Liu Z K 2010 Effects of alloying elements on elastic properties of Ni₃Al by first-principles calculations *Intermetallics* 18 1163–71
- [43] Ranganathan S I and Ostoja-Starzewski M 2008 Universal elastic anisotropy index *Phys. Rev. Lett.* 101 055504
- [44] Zaddach A J, Niu C, Koch C C and Irving D L 2013 Mechanical properties and stacking fault energies of NiFeCrCoMn high-entropy alloy JOM 65 1780-9
- [45] Zhao S, Stocks G M and Zhang Y 2017 Stacking fault energies of face-centered cubic concentrated solid solution alloys Acta Mater. 134 334-45
- [46] Fisher M E and Selke W 1980 Infinitely many commensurate phases in a simple Ising model *Phys. Rev. Lett.* 44 1502–5
- [47] Zhang Y H, Zhuang Y, Hu A, Kai J J and Liu C T 2017 The origin of negative stacking fault energies and nano-twin formation in face-centered cubic high entropy alloys *Scr. Mater.* 130 96–9
- [48] Niu C, LaRosa C R, Miao J, Mills M J and Ghazisaeidi M 2018 Magnetically-driven phase transformation strengthening in high entropy alloys Nat. Commun. 9 1363
- [49] Ikeda Y, Grabowski B and Körmann F 2019 Ab initio phase stabilities and mechanical properties of multicomponent alloys: a comprehensive review for high entropy alloys and compositionally complex alloys *Mater. Charact.* 147 464–511
- [50] Iyer M, Radhakrishnan B and Gavini V 2015 Electronic-structure study of an edge dislocation in Aluminum and the role of macroscopic deformations on its energetics J. Mech. Phys. Solids 76 260-75
- [51] Das S and Gavini V 2017 Electronic structure study of screw dislocation core energetics in Aluminum and core energetics informed forces in a dislocation aggregate J. Mech. Phys. Solids 104 115–43
- [52] Xu S, Smith L, Mianroodi J R, Hunter A, Svendsen B and Beyerlein I J 2019 A comparison of different continuum approaches in modeling mixed-type dislocations in Al Modelling Simul. Mater. Sci. Eng. 27 074004
- [53] Shen C, Li J and Wang Y 2014 Predicting structure and energy of dislocations and grain boundaries Acta Mater. 74 125–31
- [54] Zhu A, Jin C, Zhao D, Xiang Y and Huang J 2015 A numerical scheme for generalized Peierls-Nabarro model of dislocations based on the fast multipole method and iterative grid redistribution *Commun. Comput. Phys.* 18 1282–312
- [55] Hale L M 2018 Comparing modeling predictions of aluminum edge dislocations: semidiscrete variational Peierls-Nabarro versus atomistics JOM 70 1100–5

- [56] Shen C and Wang Y 2004 Incorporation of γ-surface to phase field model of dislocations: simulating dislocation dissociation in fcc crystals Acta Mater. 52 683–91
- [57] Mianroodi J R, Hunter A, Beyerlein I and Svendsen B 2016 Theoretical and computational comparison of models for dislocation dissociation and stacking fault/core formation in fcc crystals J. Mech. Phys. Solids 95 719–41
- [58] Liu G, Cheng X, Wang J, Chen K and Shen Y 2016 Peierls stress in face-centered-cubic metals predicted from an improved semi-discrete variation Peierls-Nabarro model Scr. Mater 120 94-7
- [59] Foiles S M and Hoyt J J 2006 Computation of grain boundary stiffness and mobility from boundary fluctuations Acta Mater. 54 3351–7
- [60] Warlimont H and Martienssen W (ed) 2018 Springer Handbook of Materials Data (Springer Handbooks) 2nd edn (New York: Springer)
- [61] Carter C B and Holmes S M 1977 The stacking-fault energy of nickel Phil. Mag. A 35 1161-72
- [62] Plimpton S 1995 Fast parallel algorithms for short-range molecular dynamics J. Comput. Phys. 117 1–19